

Research Article

Sono-photoacoustic imaging of gold nanoemulsions: Part II. Real time imaging



Bastien Arnal^{a,*}, Chen-Wei Wei^a, Camilo Perez^{a,c}, Thu-Mai Nguyen^a, Michael Lombardo^b,
Ivan Pelivanov^{a,d}, Lilo D. Pozzo^b, Matthew O'Donnell^a

^a University of Washington, Department of Bioengineering, 616 NE Northlake Place, Seattle, WA 98105, United States

^b University of Washington, Department of Chemical Engineering, Box 351750, Seattle, WA 98195-1750, United States

^c University of Washington, Applied Physics Laboratory, Center for Industrial and Medical Ultrasound, 1013 NE 40th Street, Seattle, WA 98105-6698, United States

^d International Laser Center, Moscow State University, Moscow, Russian Federation

ARTICLE INFO

Article history:

Received 30 October 2014

Received in revised form 31 December 2014

Accepted 11 January 2015

Keywords:

Photoacoustic cavitation

Vaporization

Gold nanoparticles

Nanoemulsion

Non-linear photoacoustics

Background suppression

ABSTRACT

Photoacoustic (PA) imaging using exogenous agents can be limited by degraded specificity due to strong background signals. This paper introduces a technique called sono-photoacoustics (SPA) applied to perfluorohexane nanodroplets coated with gold nanospheres. Pulsed laser and ultrasound (US) excitations are applied simultaneously to the contrast agent to induce a phase-transition ultimately creating a transient microbubble. The US field present during the phase transition combined with the large thermal expansion of the bubble leads to 20–30 dB signal enhancement. Aqueous solutions and phantoms with very low concentrations of this agent were probed using pulsed laser radiation at diagnostic exposures and a conventional US array used both for excitation and imaging. Contrast specificity of the agent was demonstrated with a coherent differential scheme to suppress US and linear PA background signals. SPA shows great potential for molecular imaging with ultrasensitive detection of targeted gold coated nanoemulsions and cavitation-assisted theranostic approaches.

Published by Elsevier GmbH. This is an open access article under the CC BY-NC-ND license (<http://creativecommons.org/licenses/by-nc-nd/4.0/>).

1. Introduction

Photoacoustics (PA) can leverage the optical spectra of endogenous molecular absorbers in the body to provide image contrast. For example, hemoglobin is a fairly efficient optical absorber that can be used to image the vasculature in tissue [1]. Moreover, the oxygen saturation of hemoglobin can be measured using PA spectroscopy [2] to provide functional information [3]. However, the efficiency of PA signal generation makes it very difficult to acquire single shot images for deep targets, and it is difficult to distinguish endogenous PA sources because of a number of instrumental issues. For example, there are significant artifacts in reconstructed images unless a full 3-D tomography setup is used with unblocked access to all acoustic sources and wideband transducers at sufficient density to capture all spatial frequencies [4–6]. More practical setups for medical applications using ultrasound (US) arrays are further limited

because of the finite bandwidth of these devices. Large optical absorbers (typically a few wavelengths at the central frequency) cannot be imaged correctly because the emitted low frequency content is out of the bandwidth of regular transducers, which results in high-pass filtering of the PA image. Generally, it amplifies heterogeneities and can create speckle images, typical for US images. This makes it nearly impossible to distinguish small resolved absorbers from large derivative ones. Finally, endogenous signal contrast provides limited specificity in differentiating the molecular source of the PA signal, especially at depth where wavelength dependent scattering limits the effectiveness of multi-spectral techniques [7,8]. With recently developed fast wavelength-tuning lasers, it has been shown that multi-spectral imaging can be done in real-time, providing a high level of specificity for contrast agents [9]. However, accurate reconstruction usually requires a tomographic approach using a large number of transducers for an environment where optical scattering does not greatly change the illumination pattern for different wavelengths.

To overcome some of the practical limitations of endogenous contrast, nanoparticle-based agents providing exogenous contrast and molecular targeting have been proposed [10]. For example,

* Corresponding author. Tel.: +1 2062218330.

E-mail address: bastien.arnal@gmail.com (B. Arnal).

plasmonic absorbers targeted to specific molecular biomarkers can help identify, and potentially quantify, tumor cells [11–15]. Their very small size (10–200 nm) means that they have a better probability to penetrate into any tissue from primary vessels (with typical endothelial gaps of 100 nm). However, since the PA image relies on the conversion of optical absorption into thermal expansion around the absorber to generate an US wave, a low agent concentration cannot be distinguished from surrounding endogenous absorbers. For many applications, a background suppression strategy must be used to isolate signals of interest [12,16–18], greatly improving the contrast specificity of the targeted agent.

Different kinds of non-linearities can be used to enhance both the sensitivity and contrast specificity of PA imaging [19–29]. Here we focus on a highly non-linear nanoagent that can be distinguished from surrounding linear absorbers. This non-linearity is directly related to a phase transition greatly enhancing thermal expansion, thus PA efficiency. In our previous work [23], we introduced vaporization-enhanced PA imaging of nanoemulsion beads containing perfluorohexane and coated with clusters of gold nanospheres (NEB-GNS). The amplitude of background PA signals increasing linearly with laser fluence can be easily distinguished from the much more rapidly growing nonlinear response of NEB-GNS. The advantage of this agent is a lower boiling point ($\sim 60^\circ\text{C}$) compared to that of the tissue background, avoiding thermal damage of surrounding tissue. However, a clear distinction between linear and non-linear behavior was shown for relatively high laser fluences that limit the application of this technique to depths of about 1 cm in turbid tissue.

The combination of light and ultrasound was previously introduced under the term “photoacoustic cavitation” to facilitate vapor bubble formation around plasmonic nanoparticles much more efficiently than using pulsed laser radiation or US excitation (applying negative pressure) alone [25–27]. In a companion paper to this submission, we presented results showing that simultaneous US and light stimulation can facilitate vaporization of nanoemulsion beads [28]. After a reversible phase transition of the perfluorocarbon core, a vaporization signal can be retrieved along with a scattered US signal from the resulting microbubbles. The phase transition threshold of NEB-GNS was shown to be much lower than the one observed with dispersed GNS in water (10-fold decrease in laser fluence at 1 MPa peak negative pressure for 1.2 MHz US insonification), and the combination of light and sound induced the phase transition within MPE limits for both US and laser light: the US mechanical index (MI) was below 1.9 with a laser fluence corresponding to centimeter-scale penetration into tissue within the limit of $25\text{ mJ}/\text{cm}^2$ on the skin for the 750 nm optical wavelength used in those studies.

In that previous paper, we used a 1.2 MHz focused, single-element transducer to excite the emulsion and a home-made ultra wide-band PVDF transducer to detect generated US signals. This is not a useable tool for potential clinical applications. A phase transition in the nanoemulsion can be reached at pressures of a few MPa and laser fluences of a few mJ/cm^2 . Therefore, real-time imaging using a conventional US array both for excitation of the emulsion and for reception of generated US signals is investigated here. The goal is to develop an imaging protocol combining ultrasound and laser pulses to vaporize the nanoemulsion and produce highly sensitive and specific images of this agent. To demonstrate its potential utility even at very low concentrations, we present a specific imaging sequence we call sono-photoacoustic imaging (SPA) that can easily detect NEB-GNS at pM concentrations. Moreover, we show that the SPA signal can be retrieved even with a band-limited array thanks to heterogeneities in the PA efficiency profile and acoustic properties in the bubble distribution. A tomographic reconstruction is no longer needed to

eliminate artifacts from out-of-plane sources since vaporization locations are within the imaging plane. Some alternative strategies, including spatial control of cavitation, are also proposed.

2. Material and methods

2.1. Nanoemulsion samples

NEB-GNSs were synthesized using the procedure described in previous reports [28–31]. Colloidal GNSs (diameter 12 nm) were functionalized using PEG-thiol and butane-thiol (Sigma–Aldrich, St. Louis, MO, USA), with dosages of 0.8 chains/ nm^2 Au and 700 molecules/ nm^2 Au respectively. A solution of 1 vol.% perfluorohexane (Sigma–Aldrich) and 0.012 vol.% Au clusters in water was sonicated (102C, Branson, Danbury, CT, USA, pulse regime – 1 s on, 4 s off) for 13 s in a cold water bath.

The resulting size distribution of the beads was measured by dynamic light scattering (Malvern Zetasizer Nano ZS, 633 nm wavelength, Malvern, UK). The intensity distribution was centered at a bead diameter of 129 nm with full width at half-maximum of 190 nm. This primary DLS peak ends around 500 nm. As was the case with the samples used in our companion publication, a secondary peak was present between 3 and 6 μm .

We then used another technique to purify the sample from large droplets by one-pass extrusion through a 400 nm membrane (model no. 110605, Whatman, Clifton, NJ, USA). The sample was first diluted 35 \times . To confirm and quantify the absence of large droplets, the size distribution and concentration of the emulsion were obtained prior to all experiments using a Coulter Multisizer III (Beckman Coulter, Miami, FL). A 20 μm aperture was used, which can size particles with diameters from 0.56 to 12 μm and considers any count below 0.56 μm as the noise level. The sample was diluted $\sim 1250\times$ on a 0.2 μm filtered ISOTON II electrolyte (Beckman Coulter, Miami, FL). A 50 μL sample was analyzed each time, and all measurements were repeated 6 times using a volumetric count mode. Individual particles were sized and binned in 300 evenly spaced bins with 0.039 μm width. All data are reported as a histogram with count vs. diameter, with the count (bin height) showing the number of particles in each bin interval. The reported concentration is computed for all ranges in question and accounts for the dilution factor and sampling volume used above.

A solution of molecular dye (IR-783, Sigma–Aldrich) and a solution of single GNS (12 nm diameter) were used as control samples. Absorbance spectra for all samples were measured with a spectrophotometer (UV 1601, Shimadzu, Kyoto, Japan). Normalized spectra for the two nanoemulsion samples and the two controls are presented in Fig. 1b. As shown in previous work [23,24,28–31], NEB-GNS (blue curve) and filtered NEB-GNS (black-dashed curve) have a broader tail due to plasmonic coupling between gold nanospheres. The NEB-GNS and filtered NEB-GNS were diluted to a low absorption coefficient so that there was minimal thermal coupling or interaction between resultant microbubbles from neighboring particles, ensuring that the solution response is dominated by the sum of individual nanoparticle responses to light/US excitation [32]. Consequently, all nanoemulsion samples, and the dye control sample, were diluted to an absorbance of 0.05 cm^{-1} at the operating wavelength of 750 nm (see Fig. 1a), corresponding to a solution with mean distance between each nanoemulsion bead of 7 μm and independent particle behavior in terms of thermal coupling and bubble growth dynamics. There is no thermal coupling when the light is absorbed because the distance is too large for individual thermal fields to interact, the bubbles are likely to grow and condense back without colliding, stabilizing the droplet distribution. The amount of GNS in the resulting NEB-GNS solution was then estimated. A pure GNS

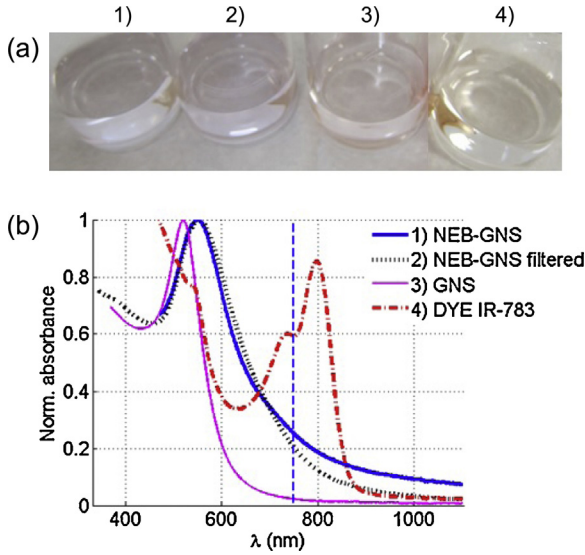


Fig. 1. (a) Photograph of different samples at the dilution used in these experiments. (b) Absorbance of the samples. (1) NEB-GNS (thick blue line), (2) NEB-GNS filtered (black dotted line), (3) GNS (12 nm diameter, thin pink line), (4) dye IR-783 (red dash dotted line). All samples were diluted so their extinctions at 750 nm are 0.05 cm^{-1} , except for the GNS solution, which has an extinction of 0.009 cm^{-1} with same amount of GNS as in the NEB-GNS. The vertical blue dotted line indicates the operating wavelength of this study (750 nm).

solution was diluted to match this total amount of gold, producing a solution with an extinction coefficient of only 0.009 cm^{-1} and a mean distance of $1.7 \mu\text{m}$ between GNS. This distance should prevent thermal coupling between GNS. For the results presented in Figs. 3–5 and 9, the solution was placed in an optically and acoustically transparent transfer pipette (3 ml, BD Falcon, NJ, USA) with inlet and outlet tubing to fill the container and remove bubbles.

2.2. Phantom preparation

For the results presented in Figs. 6–8, a polyacrylamide gel was synthesized with some nanoparticles or dye in the mixture. A first solution of 5.1 ml was prepared with 78.4% of acrylamide/bis-acrylamide solution (19:1, 40% (w/v)), 1.96% of ammonium persulfate solution (10% (w/v)) and 19.6% of trishydroxymethylaminomethane solution (buffer, pH = 8). Solutions of each nanoparticle/dye were first diluted and volumes of 0.98 ml were added to volumes of 1.02 ml of the first solution. The resulting nanoparticle/dye absorbance was matched to 0.025 cm^{-1} , except for the GNS, which was 0.0045 cm^{-1} (same amount of GNS as in the NEB-GNS). The resulting concentration of NEB-GNS was 6.3 pM . Again, the nanoparticle concentration was low enough to ensure independent particle behavior, but was high enough so that there would be sufficient SNR in measured signals to easily identify the vaporization-enhanced signals of NEB-GNS within the phantoms. Once the four solutions were placed in flat bottom wells (diameter 25 mm), 0.05% of tetramethylethylenediamine (TEMED) was added to initiate polymerization, which started within 10 min. The sample was left overnight at room temperature with a cover to allow full polymerization. Tiles of $5 \text{ mm} \times 10 \text{ mm} \times 25 \text{ mm}$ were cut from each piece of polyacrylamide and placed at the surface of a 1% agarose gel with 0.2% cellulose acting as US scatterers. The rest of the agarose solution was poured to surround each polyacrylamide inclusion with a 2 mm layer on the top.

2.3. Experimental setup and time sequence

A linear array (L7-4, 128 elements, ATL, Bothell, WA, USA) was controlled by a programmable ultrasound scanner (Vantage 128,

Verasonics, Redmond, WA, USA) operating in a custom interleaved PA – US sequence. The maximum voltage of 96 V was used to maximize the pressure amplitude. A 532-nm pump beam was injected into a wavelength-tunable optical parametric oscillator (OPO) cavity (Surelite OPO plus, Continuum, Santa Clara, CA, USA) to produce 10-ns duration, 750-nm laser pulses. Before coupling the laser beam into a fiber bundle (77526, Oriel Instruments, Stratford, CT, USA) for delivery to the sample, the fluence was adjusted with a combination of neutral density filters (NE01A-10A, Thorlabs, NJ, USA) that can be remotely switched with a six-position filter wheel (FW-103, Thorlabs, NJ, USA). A trigger signal repeated at 20 Hz was sent from a function generator (AFG-3252, Tektronix, OR, USA) both to the flash lamp trigger input of the laser and to the trigger input of the Verasonics. By adjusting delays with the Verasonics software, events involving the laser were set to start $250 \mu\text{s}$ after the flash lamp signal. A trigger output was sent to the Q-switch at each event involving the laser. This synchronized the lasing time with the reception of radiofrequency (RF) signals to cancel electronic jitter occurring if the Verasonics is triggered directly by the Q-switch ($0.2 \mu\text{s}$ in this case). The imaging sequence consisted of an US image obtained by ultrafast imaging [33] with coherent compounding [34] of 6 plane waves tilted at different angles (-5° to 5° , not depicted in Fig. 2). Then, the sono-photoacoustic acquisition (see Fig. 2a) consisted of:

- **PA**: frame using laser only excitation (*optional* for SPA)
- **US⁺**: US frame with N cycles emission (3 MHz) and positive polarity with no laser firing
- **US⁻**: US frame with N cycles emission (3 MHz) and negative polarity (opposite amplitude) with no laser firing
- **(PA + US⁺)**: laser + US image with N cycles US emission (3 MHz) and positive polarity
- **(PA + US⁻)**: laser + US image with N cycles US emission (3 MHz) and negative polarity

A lipstick hydrophone (aperture: $200 \mu\text{m}$, SEA, Soquel, CA, USA) was used to validate the timing sequence, *i.e.* lasing time relative to acoustic propagation. The combination of pulsed light and US is depicted in Fig. 2b. For the $(\text{PA} + \text{US}^\pm)$ acquisitions, light emissions are performed when the US pulse reaches a desired depth z_2 .

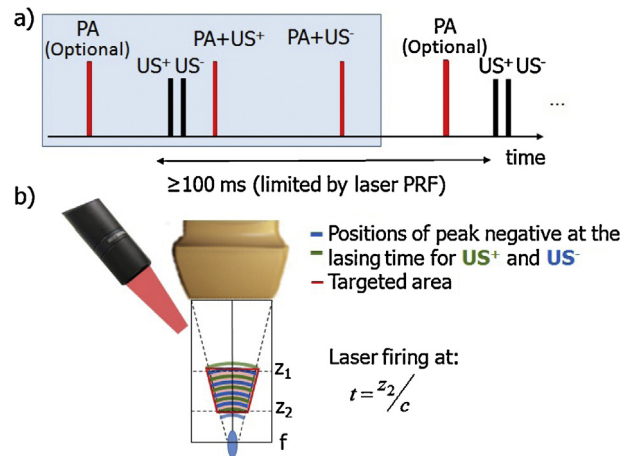


Fig. 2. Sono-photoacoustic imaging setup using a Verasonics scanner and a diagnostic ultrasound probe in wide beam mode. (a) Timing diagram. Note that PA firings can be removed in a real-time sequence since SPA does not use images formed with the laser excitation alone. (b) Imaging setup: the laser pulse emission occurs when US reaches a depth of z_2 resulting in a targeted area between z_1 and z_2 and delimited by the path of the US beam (indicated in red). A focused beam is used in the region before the focus to enhance the pressure amplitude while keeping a wide area under consideration. The blue and green lines indicate respectively where the positive and negative US peaks are at the lasing time.

The emulsion nanodroplets are vaporized or cavitated at the lasing time and at all locations of peak negative pressure [24] if combinations of acoustic pressure and laser fluence pulses are used together at diagnostic exposures. Inverting the polarities will have a complementary effect on the locations of the vaporization sites. SPA images are formed by the following coherent combination (1):

$$SPA = \{(PA + US^+) - US^+\} - \{(PA + US^-) - US^-\} \quad (1)$$

The role of both subtractions $(PA + US^\pm) - US^\pm$ is to cancel the US backscatter from tissue and isolate signals specific to the vaporization of the contrast agent. However, a linear PA signal (e.g., signal from the optical absorbers without any phase conversion) remains in both terms. The subtraction of both terms ensures that the linear PA signal is canceled while the combination of both vaporization signals is complementary since the location of peak negative pressures are offset by half of the US wavelength. A step by step demonstration of this approach is given in Section 3.1. Note that the coherent combination (1) can be equivalently performed on RF signals before or after beamforming, as it is a linear operation. In both cases, the beamforming algorithm must use one-way delays since acoustic sources of interest are formed at the lasing time.

It is possible to use this mode with plane wave insonification (see Section 3.4). However, to maximize the penetration of the technique, which is limited by the in-depth decay of laser fluence, the pressure amplitude resulting from a plane wave might not be optimal, at least with a conventional probe connected to a regular power supply. As shown in Fig. 2b, a wide-beam technique is introduced using a focused beam but the laser pulse intersects the US wave in a region prior to the transducer focus. The wide beam can enhance the pressure amplitude compared to a plane wave while conserving large coverage over a given area of interest. A maximum voltage of 96 V without apodization on transmit was applied to the L7-4 array for all results, producing a focal pressure of 3.5 MPa and pre-focal pressure (location of the SPA ROI, hydrophone at 35 mm depth) between 1.1 MPa (focus at 100 mm) and 1.9 MPa (focus at 50 mm), which was measured using a calibrated hydrophone (lipstick, aperture: 200 μm , Specialty Engineering Associates, Soquel, CA).

2.4. Transmission and reception bandwidth

US signals were sent at 3 MHz for SPA acquisitions. This frequency is at the edge of the bandwidth of the L7-4 array. The RF data were received within the bandwidth of [4–7] MHz with a high pass filter at a cutoff frequency of 3.5 MHz and implemented with Verasonics software. This made it possible to reduce linear US components scattered by bubbles over multiple cycles that can degrade axial resolution.

3. Results

3.1. SPA imaging in solutions of NEB-GNS and control samples

The four solutions prepared according to Section 2.2 were imaged using the SPA algorithm described above. An 8-cycle US excitation at 3 MHz and focused at 50 mm synchronized with lasing was used. In all cases, the fluence was set to 3.65 mJ/cm^2 and the pressure measured at 35 mm depth was 1.9 MPa (wide-beam focusing to depth of $z = 50$ mm). Fig. 3 demonstrates all radio frequency (RF) signals needed to form an SPA image and recorded for an NEB GNS solution at one of the linear array channels.

Fig. 3a illustrates a very small PA signal generated inside the pipet with NEB GNS solution. The spike around 35 μs corresponds to the PA signal created at the front surface of the pipet due to small

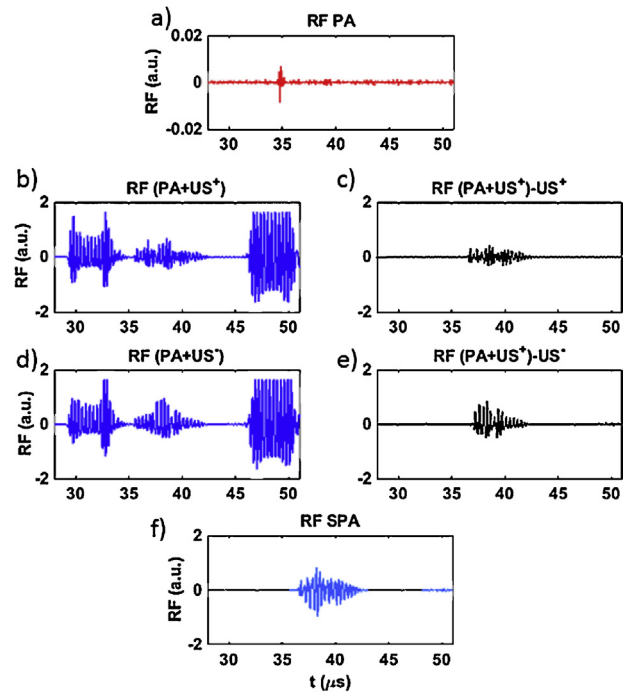


Fig. 3. RF signals from one of the array channels for NEB-GNS solution. (a) PA signal, (b) $(PA + US^+)$ signal, (c) subtraction of (b) with US^+ signal, (d) $(PA + US^-)$ signal, (e) subtraction of (c) with US^- signal, (f) SPA signal. An 8-cycle US excitation at 3 MHz is used and focused to 50 mm synchronized with lasing. In all cases, the fluence is 3.65 mJ/cm^2 and the pressure measured at 35 mm depth is 1.9 MPa.

absorption of laser radiation inside the wall and/or emulsions beads attracted to the wall. To avoid the influence of the wall on the main signal from the emulsion, the pipet had a diameter bigger than the region of light and sound interaction (~ 10 mm (laterally) \times 4 mm (axially)), which was centered at the middle of the pipet. In any event, even this wall signal was two orders of magnitude smaller than US and resulting SPA signals shown below. Thus, we can claim that the linear PA response of NEB GNS solution (e.g., without phase transition) was not recognizable from noise at the current level of emulsion concentration.

The RF signals recorded for combined US and laser excitations but for US “+” and “-” polarities are correspondingly shown in Fig. 3b and c. Strong reflections from pipet walls are observed (the signals arriving at ~ 32 μs and 47 μs), but a signal induced by simultaneous light and sound excitation is clearly seen between the pipet wall signals. This indicates that the phase transition in the emulsion droplet produces a large cavitation/vaporization signal. It is around 3 orders of magnitude bigger than the linear PA signal (e.g., without phase transition) produced at the same location with laser excitation alone, which was hardly recognizable from noise in Fig. 3a.

The coherent subtraction of the same polarity US signals, but with $(PA + US^+)$ and without (US^+) laser, gives the signals shown in Fig. 3d and e. This procedure removes the linear US signal, which is not specific to the emulsion. Here, for example, strong US wall signals are almost completely suppressed. However, the linear PA signal would be still visible if it was not so small. The SPA signal illustrated in Fig. 3f is calculated to retrieve a NL sono-photoacoustic signal composed of vaporization and cavitation activity signatures occurring specifically at the nanoemulsion bead location.

This same procedure was applied to all four samples. Fig. 4 represents the evolution over multiple frames of the mean SPA image amplitude inside a 3 mm \times 3 mm region for different solutions. SPA signals in all solutions are quite consistent in time. This indicates that the vaporization process does not destroy

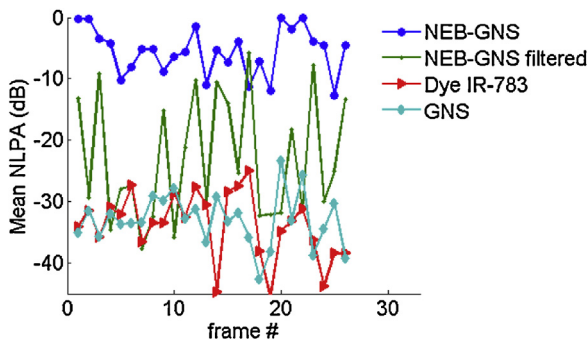


Fig. 4. Mean SPA amplitude in a 3 mm \times 3 mm region over multiple frames. Solution types are indicated in the legend.

nanodroplets: the emulsion beads condense back to the liquid state a few microseconds after the excitation has been completed. Thus, the excitation is non-destructive and reversible for the emulsion. The green curve with small dot marker shows that the signal enhancement from the absence and presence of vaporization is about 20 dB in this case. For a slightly higher fluence (not shown here), it is possible to obtain consistent signal enhancement with this sample.

Images have been recorded at a frame rate of 1.3 Hz to allow RF and beamformed data to be saved simultaneously. If this saving operation is not performed, the display rate can be greatly improved up to 7 Hz (or 10 Hz without the linear PA image).

A single SPA image of the NEB-GNS solution superimposed on the US B-scan is presented in Fig. 5a. The solution concentration was estimated to be 12.6 pM. For the NEB-GNS filtered sample shown in Fig. 5b, signal enhancement can be obtained at the same exposure but not with a probability of 1 and within a smaller area. This is consistent with the results of our companion publication, which shows that both the vaporization threshold and signal enhancement depend on the size of the droplets. The reference sample, dye and GNS (Fig. 5c and d, correspondingly) do not show any signal enhancement among the 28 frames acquired for the current values of laser fluence and US excitation pressure. Hence, for NEB-GNS, signal enhancement of 35 dB appears when the cavitation threshold is reached, which could be very useful for real-time detection of low nanoagent concentrations.

Note here, that SPA imaging can retrieve signal from the inside of a large homogeneous absorbing solution even when a band-limited array (4–7 MHz) is used. The formed bubbles induce a

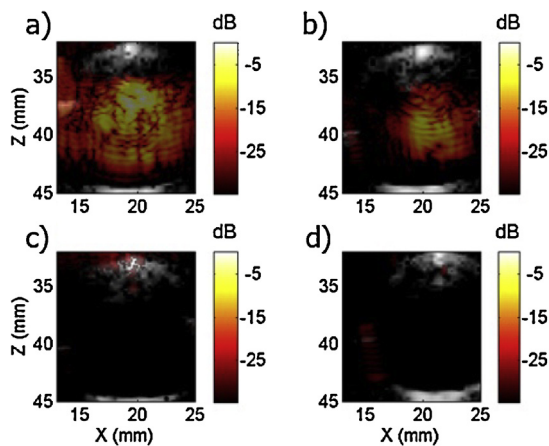


Fig. 5. Sono-photoacoustic imaging of different absorbing solutions at ultra-low concentrations. (a) NEB-GNS, (b) NEB-GNS filtered, (c) molecular dye IR-783 and (d) GNS-12 nm with a matching amount of gold particles as in NEB-GNS.

highly heterogeneous PA source distribution with large fluctuations in thermal expansion as well as heterogeneous acoustic properties, producing a speckle image. In contrast, a linear PA image would lead to signal only at the bottom/top of the pipette and at much lower amplitude given the dilution of the samples.

3.2. SPA imaging of NEB-GNS in polyacrylamide phantom

A PA signal can be seen at 33 μ s (cf Fig. 6a) for the polyacrylamide gel infused with NEB-GNS. It comes from an acoustic absorber plate (blue color) that also absorbs light and generates a linear PA signal. No linear PA signal from the NEB-GNS was measured above the noise floor.

The combination of light and sound for both US polarities using 8-cycle emissions at 3 MHz focused at 60 mm can be observed in Fig. 6b and c. The laser fluence was 5.2 mJ/cm² and the acoustic peak negative pressure measured at $z = 35$ mm was 1.6 MPa (wide-beam focusing at 60 mm). The RF signals in Fig. 6b and c include the PA signal at 33 μ s but it is hidden by the US backscatter. Subtraction of the same polarity US signals, but obtained with laser, (PA + US⁺), and without the laser, US⁺, gives the signal shown in (d). It shows a difference in the response of the emulsion created by adding the laser pulse to the 8-cycle 3 MHz US signal. When the response of the emulsion is linear, this differential signal should be equal to the PA one illustrated in Fig. 6a. However, combining laser and US creates a phase transition in the emulsion beads resulting in a nonlinear contribution formed by bubble thermal expansion and nonlinear scattering of the probe 8-cycle US signal by the bubbles.

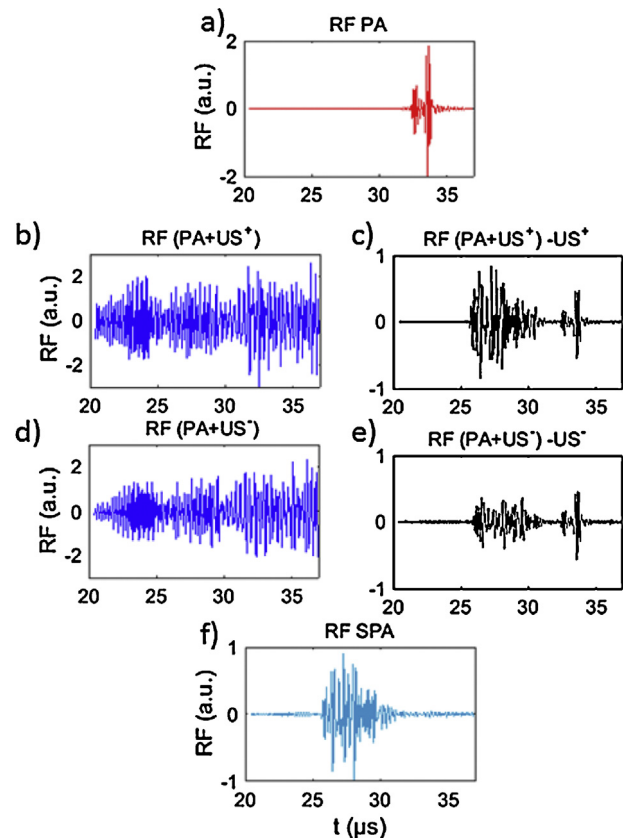


Fig. 6. RF signals from one of the array channels for the phantom with a NEB-GNS polyacrylamide inclusion located inside an agarose gel. (a) PA signal, (b) (PA + US⁺) signal, (c) (PA + US⁻) signal, (d) subtraction of (b) with US⁺ signal, (e) subtraction of (c) with US⁻ signal, (f) SPA signal. An 8-cycle US excitation at 3 MHz and focused to 60 mm was synchronized with lasing. The acoustic pressure measured at 35 mm is 1.6 MPa; the laser fluence is 5.2 mJ/cm².

Fig. 6e shows the residual signal $(PA + US^-) - US^-$, similar to that illustrated in Fig. 6d, but obtained with the US^- excitation, i.e. with the signal inverted in polarity compared to US^+ . Since the phase transition in the emulsion occurs at positions with maximum negative pressure (corresponding to the 8 negative peaks of the US excitation), bubbles will be formed at different locations compared to the one obtained with the US^+ excitation. Note that in both Fig. 6d and e the linear PA signal around $33 \mu s$ is preserved. The final SPA signal in Fig. 6f is obtained by subtracting Fig. 6d and e. It suppresses all linear PA and US background signals not related to cavitation activity of the nanoemulsion.

Fig. 7 presents images summarizing these results on the phantom. Fig. 7a shows a conventional US image, it was obtained with the same linear array, but used the whole transducer bandwidth in conventional imaging mode. The inclusion is seen as a black rectangle (see Fig. 7a). The surrounding medium was an agarose phantom with US scatterers providing speckles. The bright line situated at the bottom of the gel in the right corner corresponds to a blue acoustic absorber plate (AptFlex F28, Precision Acoustics, Dorchester, UK) placed here to reduce US reflections from the bottom of the container that could create reverberation throughout the container. The SPA image corresponds to a signal coming from the inclusion containing NEB-GNS (see Fig. 7c). This imaging sequence can suppress linear PA and US signals to retrieve the NL sono-photoacoustic signal composed of vaporization and cavitation activity signatures occurring specifically at the nanoemulsion bead location. In Fig. 7d, the SPA image (hot colorbar) is overlaid onto the US image obtained in Fig. 7a.

3.3. Comparison of SPA images in polyacrylamide phantom for NEB-GNS with GNS and dye samples

Images for the agarose phantom containing 4 polyacrylamide inclusions are shown in Fig. 8: NEB-GNS (a), NEB-GNS filtered (b), dye-783 (c) and GNS (d). In these figures, the SPA image (hot colorbar) is overlaid onto the US picture (displayed over a 40 dB dynamic range) and the maximum signal from the NEB-GNS inclusion is considered as a reference (0 dB) for all other SPA images. In all cases, the linear PA signal coming from the absorber was canceled except a small residual visible in (b) that could correspond to a change in optical scattering due to varying bubble clouds between the two $(PA + US)$ images or simply pulse energy fluctuation. However, the SPA image amplitude is generally much greater than the residuals and can clearly be identified without signal averaging. The average (over the inclusion) contrast between the inclusion and the gel in the image (in dB) was respectively 21.0 dB, 8.3 dB, -7.3 dB and -19 dB for the four

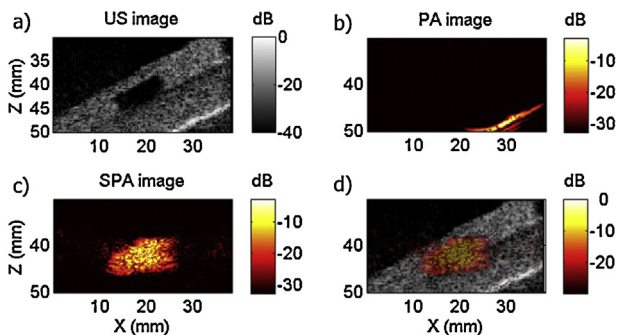


Fig. 7. SPA imaging of a NEB-GNS polyacrylamide inclusion located inside an agarose gel: (a) ultrasound image, (b) PA image, (c) SPA image and (d) SPA image overlaid on the US image. An 8-cycle US excitation at 3 MHz and focused to 60 mm was synchronized with laser. The acoustic pressure measured at 35 mm is 1.6 MPa, and the laser fluence is 5.2 mJ/cm^2 .

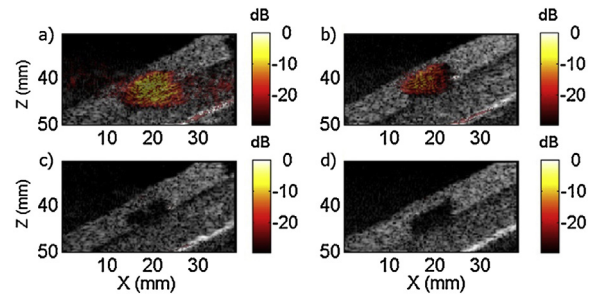


Fig. 8. SPA imaging of different agents embedded into polyacrylamide inclusion located inside an agarose gel: (a) NEB-GNS, (b) NEB-GNS filtered, (c) GNS-12 nm with the same amount of gold as NEB-GNS and (d) molecular dye IR-783 nm. The reference magnitude (0 dB) corresponds to the maximum of the SPA image. The laser fluence was 5.2 mJ/cm^2 and the acoustic peak negative pressure measured at $z = 35 \text{ mm}$ was 1.6 MPa (wide-beam focusing at 60 mm).

samples. The contrast to noise ratio (CNR) for the two phantoms with measurable SPA contrast was respectively 26.8 dB and 18.4 dB, enabling clear identification of the agent.

3.4. High resolution SPA imaging in solutions of NEB-GNS with a single-cycle US wave

Multiple cycle US pulses were used to cover a large area at once. However, as shown in the companion paper [28], a laser-US nucleated bubble may keep oscillating over the remaining US pulse. The presence of an US field creates a bubble oscillation preventing re-condensation. It can result in degraded axial resolution since the bubbles backscatter until they condense or collapse. As an alternative, a single-cycle US pulse can be used, as shown in Fig. 9. In this example, a plane wave of 1.03 MPa (measured at a 35 mm depth) was emitted by the array and the laser fluence was set to 3.3 mJ/cm^2 . Three frames recorded at different times in a continuous imaging sequence for the same conditions are displayed (panels a–c). The SPA signal is a horizontal stripe and no signal comes from either side. The position of the SPA signal is very stable in time and depends only on the timing of the laser pulses relative to propagation of the plane wave. It shows that the SPA method can fully control the cavitation location for applications such as drug delivery, molecular imaging, or therapy [35], with the potential for minimal impact to vital healthy surrounding tissues. If multiple areas are to be investigated or treated, the delay between laser and US emissions can be scanned and multiple images can be combined.

4. Discussion

This paper presents an imaging mode called sono-photoacoustics (SPA imaging) that can achieve ultrasensitive and specific

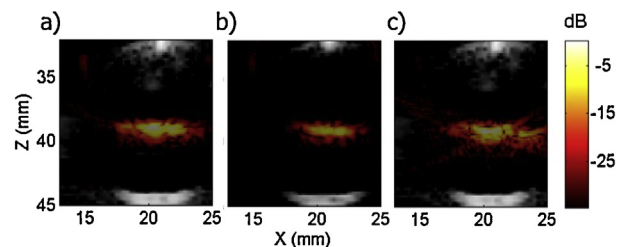


Fig. 9. SPA obtained for NEB-GNS solution using a single-cycle US excitation. Panels (a–c) correspond to the detection at three different times in a continuous imaging sequence for exactly the same configuration. US plane wave of 1.03 MPa (measured at a 35 mm depth) is used for the excitation together with the laser fluence of 3.3 mJ/cm^2 .

imaging of nanoagents at low concentrations (below 7 pM). The signal enhancement and sensitivity of the technique come from exploiting phase transitions of nanodroplets under combined low US exposure and pulsed-laser excitation. A phase transition is induced by heat around the plasmonic absorber combined with refractive pressure. There are two consequences of combining light with sound. On one hand, a phase transition can be achieved at lower exposures than for only one type of field, US or optical. On the other hand, the US field during a phase transition in the vicinity of the bubble is immediately back-scattered from the high acoustic impedance mismatch.

Previous research focused on ultrasound-only vaporization for therapeutic and imaging applications, demonstrating B-mode imaging of the acoustic droplet vaporization process *in vivo* [36,37] and stability of similar droplets *in vivo* for at least several hours prior to imaging. However, continuous wave US excitation for 60 s was required for vaporization at high US pressures, causing more than 15 °C temperature increase for this process to be successful. SPA imaging reduces the pressure required by locally reducing surface tension at the droplet surface, thus avoiding the widespread temperature increase caused by CW excitations. As shown in Fig. 9, SPA requires just one or a few US cycles at low pressures, combined with light, to visualize and localize the emulsion inside a biological target.

We have demonstrated this principle with highly diluted samples (picomolar range), implying that the linear PA signal was too small to be measurable. Results show that a high contrast of around 30–40 dB can be obtained between areas with and without nanodroplets due to coherent suppression of linear and NL US, and linear PA signals. However, the fluence used to obtain these results is slightly higher than the one used in the companion paper where we could observe vaporization with 0.6 mJ/cm². This is due to a change of US excitation frequency from 1 MHz to 3 MHz. Unless superharmonic focusing still dominates using photoacoustic vaporization [38], the thresholds are expected to increase with frequency since, using short US bursts, mechanical effects dominate *i.e.* effects related to the mechanical index (MI). The acoustic pressure could not be increased because of the limited maximum voltage provided to the ultrasound scanner used for this study. We traded off a low excitation frequency to demonstrate that SPA imaging could be performed at high spatial resolution using a single array transducer. These preliminary results are promising, but other solutions using lower frequency external sources will be tested as well.

The current implementation may have challenges in terms of physiological motion robustness for *in vivo* applications. Indeed, coherent subtraction using a laser repetition rate of 20 Hz cannot be applied *in vivo* in organs affected by respiration or cardiac-induced motion. While each US image can be acquired right after each PA + US image, allowing proper subtraction, the linear PA signal will remain in the end and the combination of the two images $(PA + US^+) - US^+$ and $(PA + US^-) - US^-$ cannot be coherently combined without artifacts if there is significant motion between laser pulses. In this case, ECG and breathing triggering can be applied if all motion is cyclic and stable.

The robustness of the subtraction might be improved using next generation lasers with higher repetition rates to perform the whole acquisition in less than 1 ms, which would enable *in vivo* application with minor modifications of the protocol presented here. However, if the linear PA signals are negligible or can be kept without confusion, the technique can be applied with good motion robustness because what matters most, is to subtract the $US^{+/-}$ from the $(PA + US^{+/-})$. For example, time persistence or incoherent summation can combine information obtained with the US^+ and US^- based-images but this would conserve linear PA parts. Further studies will focus on optimizing this principle for *in vivo* experiments.

In this study, detection with high contrast at a very low agent concentration was the first priority. Using a multiple-cycle excitation, the response from different bubbles is elongated in time. Once some signal has been detected in a given area, the same area can be scanned with a thinner grid using single-cycle excitation to maximize spatial resolution. To maximize axial resolution, time gating (*e.g.*, with a Gaussian window) can be applied to the signals since the *a priori* location of the US pulse at lasing is known. This approach can cancel the effect of bubble ringing. Similar issues arise for other types of nanodroplets that require long US bursts to induce a phase transition [39]. Several alternatives are currently under consideration to maintain high spatial resolution while preserving the detection sensitivity demonstrated here. In any event, the current implementation provides an extremely high level of contrast and specificity, even at pM-scale nanoagent concentrations: a single SPA image gives a SNR of 28 dB at a concentration of only 6.3 pM with a signal enhancement over 500 compared to conventional PA. The CNR reaches 26 dB, demonstrating a high level of specificity. At this concentration, the average distance between sources is far beyond the thermal diffusion distance within the laser pulse duration. PA transients can be considered as excited by isolated thermal sources. In this regime, concentration does not matter anymore and even a single nanodroplet should provide a measurable SPA signal. Direct evidence of this fact will be obtained in a forthcoming experiment

5. Conclusion

Sono-photoacoustic (SPA) imaging has been demonstrated with a conventional linear US array. This technique combines pulsed laser and US excitations of gold coated nanoemulsions resulting in local generation of cavitation bubbles due to a phase transition of the nanodroplet. This procedure can reach very high signal-to-noise ratios to image very low concentrations of contrast agent (<6 pM) where classical linear PA imaging fails, it activates spatially controlled cavitation events only in the emulsion beads, keeping the background undisturbed due to the low phase transition temperature of the perfluorocarbon, and it achieves very high imaging specificity and suppresses all linear PA and US signals from the background. A commercial band-limited diagnostic array is used both for excitation of nanoemulsions and imaging at laser fluences and negative US pressures far below MPE limits. The contrast agent itself has not been destroyed after multiple SPA frames are applied, *i.e.* cavitation bubbles condense back to the liquid state after the excitation. Spatial control of cavitation with a simple US tool may enable safe therapeutic procedures based on inertial cavitation for applications such as sono-thrombolysis and drug delivery with real-time treatment monitoring, or provide ultra-sensitive images of micro-vasculature and molecularly targeted cells using SPA processing. Thus, SPA shows great potential for molecular imaging with ultrasensitive detection of targeted gold coated nanoemulsion and cavitation-assisted theranostic approaches. Future studies will focus on such potential theranostic applications.

Conflict of interest

The authors declare that there are no conflicts of interest.

Acknowledgments

This work was supported in part by NIH RO1-EB016034, RO1-CA170734, RO1-HL121226, the Life Sciences Discovery Fund 3292512, NSF CBET-1236309, and the Department of Bioengineering at the University of Washington.

References

- [1] Hu S, Wang LV. Photoacoustic imaging and characterization of the microvasculature. *J Biomed Opt* 2010;15(1):011101.
- [2] Wang X, Xie X, Ku G, Wang LV, Stoica G. Noninvasive imaging of hemoglobin concentration and oxygenation in the rat brain using high-resolution photoacoustic tomography. *J Biomed Opt* 2006;11(2):024015.
- [3] Zhang HF, Maslov K, Stoica G, Wang LV. Functional photoacoustic microscopy for high-resolution and noninvasive in vivo imaging. *Nat Biotechnol* 2006;24(July (7)):848–51.
- [4] Ntziachristos V, Ripoll J, Wang LV, Weissleder R. Looking and listening to light: the evolution of whole-body photonic imaging. *Nat Biotechnol* 2005;23(March (3)):313–20.
- [5] Khokhlova TD, Pelivanov IM, Karabutov AA. Methods of optoacoustic diagnostics of biological tissues. *Acoust Phys* 2009;55(October (4–5)):674–84.
- [6] Ku G, Wang X, Stoica G, Wang LV. Multiple-bandwidth photoacoustic tomography. *Phys Med Biol* 2004;49(April (7)):1329.
- [7] Rosenthal A, Razansky D, Ntziachristos V. Fast semi-analytical model-based acoustic inversion for quantitative optoacoustic tomography. *IEEE Trans Med Imaging* 2010;29(June (6)):1275–85.
- [8] Jetzfellner T, Razansky D, Rosenthal A, Schulz R, Englmeier K-H, Ntziachristos V. Performance of iterative optoacoustic tomography with experimental data. *Appl Phys Lett* 2009;95(July (1)):013703.
- [9] Luis Deán-Ben X, Razansky D. Adding fifth dimension to optoacoustic imaging: volumetric time-resolved spectrally enriched tomography. *Light Sci Appl* 2014;3(January (1)):e137.
- [10] De La Zerda A, Zavaleta C, Keren S, Vaithilingam S, Bodapati S, Liu Z, et al. Carbon nanotubes as photoacoustic molecular imaging agents in living mice. *Nat Nanotechnol* 2008;3(September (9)):557–62.
- [11] Li P-C, Wang C-R, Shieh D-B, Wei C-W, Liao C-K, Poe C, et al. In vivo photoacoustic molecular imaging with simultaneous multiple selective targeting using antibody-conjugated gold nanorods. *Opt Express* 2008;16(November (23)):18605–15.
- [12] Mallidi S, Larson T, Tam J, Joshi PP, Karpouk A, Sokolov K, et al. Multiwavelength photoacoustic imaging and plasmon resonance coupling of gold nanoparticles for selective detection of cancer. *Nano Lett* 2009;9(August (8)):2825–31.
- [13] Agarwal A, Huang SW, O'Donnell M, Day KC, Day M, Kotov N, et al. Targeted gold nanorod contrast agent for prostate cancer detection by photoacoustic imaging. *J Appl Phys* 2007;102(September (6)):064701.
- [14] Song KH, Kim C, Cobley CM, Xia Y, Wang LV. Near-infrared gold nanocages as a new class of tracers for photoacoustic sentinel lymph node mapping on a rat model. *Nano Lett* 2009;9(January (1)):183–8.
- [15] Chen Y-S, Frey W, Kim S, Kruijzinga P, Homan K, Emelianov S. Silica-coated gold nanorods as photoacoustic signal nanoamplifiers. *Nano Lett* 2011;11(February (2)):348–54.
- [16] Wei C, Xia J, Pelivanov I, Jia C, Huang S-W, Hu X, et al. Magnetomotive photoacoustic imaging: in vitro studies of magnetic trapping with simultaneous photoacoustic detection of rare circulating tumor cells. *J Biophotonics* 2013;6(6–7):513–22.
- [17] Qu M, Mallidi S, Mehrmohammadi M, Truby R, Homan K, Joshi P, et al. Magneto-photo-acoustic imaging. *Biomed Opt Express* 2011;2(February (2)):385–96.
- [18] Razansky D, Distel M, Vinegoni C, Ma R, Perrimon N, Köster RW, et al. Multispectral opto-acoustic tomography of deep-seated fluorescent proteins in vivo. *Nat Photonics* 2009;3(July (7)):412–7.
- [19] Zharov VP. Ultrasharp nonlinear photothermal and photoacoustic resonances and holes beyond the spectral limit. *Nat Photonics* 2011;5(February (2)):110–6.
- [20] Nam SY, Ricles LM, Suggs LJ, Emelianov SY. Nonlinear photoacoustic signal increase from endocytosis of gold nanoparticles. *Opt Lett* 2012;37(November (22)):4708–10.
- [21] Wilson K, Homan K, Emelianov S. Biomedical photoacoustics beyond thermal expansion using triggered nanodroplet vaporization for contrast-enhanced imaging. *Nat Commun* 2012;3(January):618.
- [22] Hannah AS, VanderLaan D, Chen Y-S, Emelianov SY. Photoacoustic and ultrasound imaging using dual contrast perfluorocarbon nanodroplets triggered by laser pulses at 1064 nm. *Biomed Opt Express* 2014;5(September (9)):3042.
- [23] Wei C, Lombardo M, Larson-Smith K, Pelivanov I, Perez C, Xia J, et al. Nonlinear contrast enhancement in photoacoustic molecular imaging with gold nanosphere encapsulated nanoemulsions. *Appl Phys Lett* 2014;104(January (3)):033701.
- [24] Wei C, Xia J, Lombardo M, Perez C, Arnal B, Larson-Smith K, et al. Laser-induced cavitation in nanoemulsion with gold nanospheres for blood clot disruption: in vitro results. *Opt Lett* 2014;39(May (9)):2599–602.
- [25] Farny CH, Wu T, Holt RG, Murray TW, Roy RA. Nucleating cavitation from laser-illuminated nano-particles. *Acoust Res Lett Online* 2005;6(138).
- [26] Ju H, Roy RA, Murray TW. Gold nanoparticle targeted photoacoustic cavitation for potential deep tissue imaging and therapy. *Biomed Opt Express* 2013;4(January (1)):66–76.
- [27] McLaughlan JR, Roy RA, Ju H, Murray TW. Ultrasonic enhancement of photoacoustic emissions by nanoparticle-targeted cavitation. *Opt Lett* 2010;35(July (13)):2127–9.
- [28] Arnal B, Perez C, Wei C-W, Xia J, Lombardo M, Pelivanov I, et al. Sono-photoacoustic imaging of gold nanoemulsions: Part I. Exposure thresholds. *Photoacoustics* 2015. <http://dx.doi.org/10.1016/j.pacs.2014.12.001>.
- [29] Dove JD, Mountford PA, Murray TW, Borden MA. Engineering optically triggered droplets for photoacoustic imaging and therapy. *Biomed Opt Express* 2014;5(December (12)):4417–27.
- [30] Larson-Smith K, Pozzo DC. Pickering emulsions stabilized by nanoparticle surfactants. *Langmuir* 2012;28:11725–32.
- [31] Larson-Smith K, Pozzo DC. Scalable synthesis of self-assembling nanoparticle clusters based on controlled steric interactions. *Soft Matter* 2011;7:5339.
- [32] Matsunaga TO, Sheeran PS, Luois S, Streeter JE, Mullin LB, Banerjee B, et al. Phase-change nanoparticles using highly volatile perfluorocarbons: toward a platform for extravascular ultrasound imaging. *Theranostics* 2012;2(12):1185–98.
- [33] Tanter M, Bercoff J, Sandrin L, Fink M. Ultrafast compound imaging for 2-D motion vector estimation: application to transient elastography. *IEEE Trans Ultrason Ferroelectr Freq Control* 2002;49(October (10)):1363–74.
- [34] Montaldo G, Tanter M, Bercoff J, Benech N, Fink M. Coherent plane-wave compounding for very high frame rate ultrasonography and transient elastography. *IEEE Trans Ultrason Ferroelectr Freq Control* 2009;56(March (3)):489–506.
- [35] Vlaisavljevich E, Durmaz YY, Maxwell A, ElSayed M, Xu Z. Nanodroplet-mediated histotripsy for image-guided targeted ultrasound cell ablation. *Theranostics* 2013;3(October (11)):851–64.
- [36] Rapoport N, Nam K-H, Gupta R, Gao Z, Mohan P, Payne A, et al. *J Control Release* 2011;153(4).
- [37] Rapoport NY, Kennedy AM, Shea JE, Scaife CL, Nam K-H. *J Control Release* 2009;138(268).
- [38] Shpak O, Verweij M, Vos HJ, de Jong N, Lohse D, Versluis M. Acoustic droplet vaporization is initiated by superharmonic focusing. *Proc Natl Acad Sci U S A* 2014;111(April (5)):1697–702.
- [39] Giesecke T, Hynynen K. Ultrasound-mediated cavitation thresholds of liquid perfluorocarbon droplets in vitro. *Ultrasound Med Biol* 2003;29(September (9)):1359–65.



Bastien Arnal received his engineering degree from Ecole Supérieure de Physique et de Chimie Industrielles de Paris (ESPCI ParisTech) in 2009 with a joint M.Sc. degree in acoustics from University Paris VII. In 2007, he worked for Phillips Research North America in Briarcliff Manor, NY, on medical ultrasonics. He received his Ph.D. at Institut Langevin in Paris. He received the Nadine Barrie Smith student award at the ISTU in 2012. He is currently a postdoc in bioengineering at the University of Washington, Seattle, USA. His research interests include medical ultrasonic imaging, ultrasonic therapy, shear wave elastography, inverse problems, time-reversal and molecular imaging using photoacoustics.



Chen-Wei Wei received the B.S. degree in electrical engineering from National Chiao-Tung University, Hsinchu, Taiwan, in 2003, and the M.S. and Ph.D. degree in electrical engineering from National Taiwan University, Taipei, Taiwan, in 2005 and 2009, respectively. He is currently a postdoctoral in bioengineering at University of Washington, Seattle, USA. His current research interests include new ultrasound and photoacoustic contrast agent and new imaging techniques.



Camilo Perez is a Ph.D. student in the bioengineering program at the University of Washington in Seattle. He is a member of the Center for Industrial and Medical Ultrasound, working on his Ph.D. under the direction of Dr. Thomas J. Matula. He received B.S. degree in electrical engineering at the University of Delaware. His area of research involves extracorporeal shockwave therapy, ultrasound metrology characterization of shockwave fields, characterization of ultrasound contrast agents (microbubbles), and characterization of phase change emulsions as photoacoustic/ultrasound contrast agents. He is also the treasurer of the Seattle Student Chapter of the Acoustical Society of America (SSCASA).



Thu-Mai Nguyen was born in 1986 in France. In 2009, she received an engineering degree from the Ecole Supérieure de Physique et Chimie Industrielles (ESPCI ParisTech, France). In 2012, she received a Ph.D. degree in acoustics from the University Paris Diderot for her work on elastography of cornea and skin layers. Her research interests include ultrasound imaging and optical coherence tomography for characterization of tissue biomechanics.



Michael Lombardo received his B.S. in chemical engineering from the University of Missouri in 2012. He then began his Ph.D. research at the University of Washington in colloidal self-assembly.



Ivan Pelivanov is an Assistant Professor at the Physics faculty of M.V. Lomonosov Moscow State University and visiting Assistant Professor at the University of Washington (WA, USA). He graduated from the group of Prof. A.A. Karabutov, which is a pioneering and renowned team in various physical and biological applications of optoacoustic spectroscopy, and received his Ph.D. degree in 2000. His recent research focuses on designing sensitive wide-band detectors, application of optoacoustic method in NDT and material evaluation, analytic chemistry and in medicine. He is one of the most active members in optoacoustic research for more than a decade.



Prof. Lilo D. Pozzo is Associate Professor of Chemical Engineering at the University of Washington in Seattle. She holds a B.S. in chemical engineering from the University of Puerto Rico Mayagüez (2001) as well as a MS Degree in Colloid, Polymers and Surfaces (2006) and a Ph.D. in chemical engineering from Carnegie Mellon University (2006). She worked as a postdoctoral researcher at the NIST Center for Neutron Research and at the University of Maryland. Her research interests and expertise focus on the control and manipulation of self-assembling soft materials and their use in health, energy and engineering materials applications.



Matthew O'Donnell has worked at General Electric CRD, the University of Michigan, where he was Chair of the BME Department from 1999 to 2006, and the University of Washington (UW), where he was the Frank and Julie Jungers Dean of Engineering from 2006 to 2012. He is now Professor of Bioengineering at UW. His most recent research has focused on elasticity imaging, optoacoustic arrays, photoacoustic contrast agents, thermal strain imaging, and catheter-based devices. He is a fellow of the IEEE and AIMBE and is a member of the Washington State Academy of Sciences and the National Academy of Engineering.